Electron accumulation and charge neutrality level at the Eu/EuO interface

Lingyuan Gao, Wei Guo, Agham Posadas, and Alexander A. Demkov*
Department of Physics, The University of Texas at Austin, Austin, Texas 78712, USA

(Received 24 January 2019; revised manuscript received 2 August 2019; published 9 September 2019)

Using a combination of density functional theory and *in situ* x-ray photoelectron spectroscopy, we study the atomic and electronic structure of the Eu/EuO interface. Calculations predict that electrons transfer from Eu metal into EuO and induce an unexpected downward band bending at the interface. Accounting for spectral broadening and attenuation of the signal from subsurface layers, the calculated layer-resolved total density of states agrees well with experimental x-ray photoelectron spectroscopy in the valence-band region. The total $4f$ spectrum contains contributions from both Eu and EuO, with the latter component significantly broadened as a result of band bending. This bending and charge transfer originate from Eu *Fermi-level* pinning at the EuO charge neutrality level, which has been suggested to be located above the conduction-band bottom [Phys. Rev. B **86**, 205310 (2012)].

DOI: 10.1103/PhysRevMaterials.3.094403

I. INTRODUCTION

Europium monoxide, EuO, is a prototypical Heisenberg ferromagnetic (FM) insulator with a Curie temperature T_c of 69 K [1]. It crystallizes in the cubic rocksalt structure and at room temperature has a band gap of 1.1 eV [1]. Below T_c, the large $7\mu_B$ magnetic moment of the Eu^{2+} ions originating from the electrons in the half-filled $4f$ shell become ferromagnetically aligned. In addition to standard magnetization measurements, this local magnetization has also been probed experimentally with optical techniques utilizing the Faraday and Kerr magneto-optic effects [2,3]. Several methods have been used to enhance the Curie temperature of EuO, including both an isotropic lattice contraction and compressive biaxial strain [4,5], as well as chemical doping with trivalent rare-earth metals that can nearly double T_c [6]. Furthermore, when EuO is doped n type (for example, with Gd or when oxygen vacancies are introduced), the ferromagnetic transition is accompanied by a colossal magnetoresistance effect ($\frac{\Delta\rho}{\rho} \sim 10^6$ at 100 kOe) [7] and an insulator-metal transition ($\frac{\Delta\rho}{\rho} \sim 10^{13}$) [8,9]. Such a combination of magnetic, magneto-optical, and magnetoresistive properties makes EuO an attractive candidate for a variety of spintronic applications. In addition, EuO can be integrated epitaxially on common semiconductors such as Si and GaN [10–12], making it attractive for integrating magnetic devices directly on semiconductors. Recently, Posadas *et al.* discussed Eu metal deposition on $SrTiO_3$ (001) in the absence of oxygen [13]. It was observed that at a deposition temperature of 300 °C, Eu scavenges oxygen from the $SrTiO_3$ (STO) layers beneath, forming epitaxial EuO and leaving a conductive, oxygen-deficient STO layer below the EuO/STO interface. Because of the large exchange spin-splitting in the conduction band of EuO of ~0.6 eV, this opens up an intriguing possibility for creating a spin-filter tunnel junction comprised of EuO and its parent metal Eu to form a Eu/EuO/conductive STO heterojunction. To our knowledge, the literature on the Schottky barrier at the Eu/EuO interface is scarce; however, interfaces with other metals have been considered [14–20]. The most relevant recent study is that of Jutong and coauthors who, using complex band structure analysis, predicted that the charge neutrality level of EuO is located above the conduction-band bottom [14]. This would make the band alignment rather peculiar.

In this paper, by combining density functional theory (DFT) calculations with *in situ* x-ray photoelectron spectroscopy (XPS), we study the atomic and electronic structure of the Eu/EuO interface. The paper is organized as follows: We describe the computational and experimental methods in Sec. II. In Sec. III, we explore the potential-energy surface (PES) for the Eu adatom on the EuO (001) surface and discuss the optimal geometry for the Eu/EuO interface. In Sec. IV, the calculated electronic structure of the Eu/EuO heterostructure is described and compared with experimental XPS data. In Sec. V, the band alignment of the Eu/EuO interface and charge transfer from Eu to EuO are analyzed and discussed in detail. Section VI describes the calculated surface and interface energies, and explores the wetting conditions of EuO by Eu.

II. METHOD

We perform *ab initio* calculations using the Vienna *ab initio* simulation package (VASP) [21,22]. Due to the highly localized nature of $4f$ orbitals, the magnetic ground state of rare-earth metals cannot be properly described by either the local-spin density approximation (LDA) [23] or by the generalized gradient approximation (GGA) [24]. Consequently, two different remedies have been used in previous studies: (i) the "open-core" approach [25] or (ii) methods that include the Hubbard-type U correction in standard DFT approximations [26,27]. In the former approach, the $4f$ orbitals are not included in the valence band but are treated as part of the atomic core, which leads to the loss of band mixing between the f states and other bands. Here, we follow the latter

*demkov@physics.utexas.edu

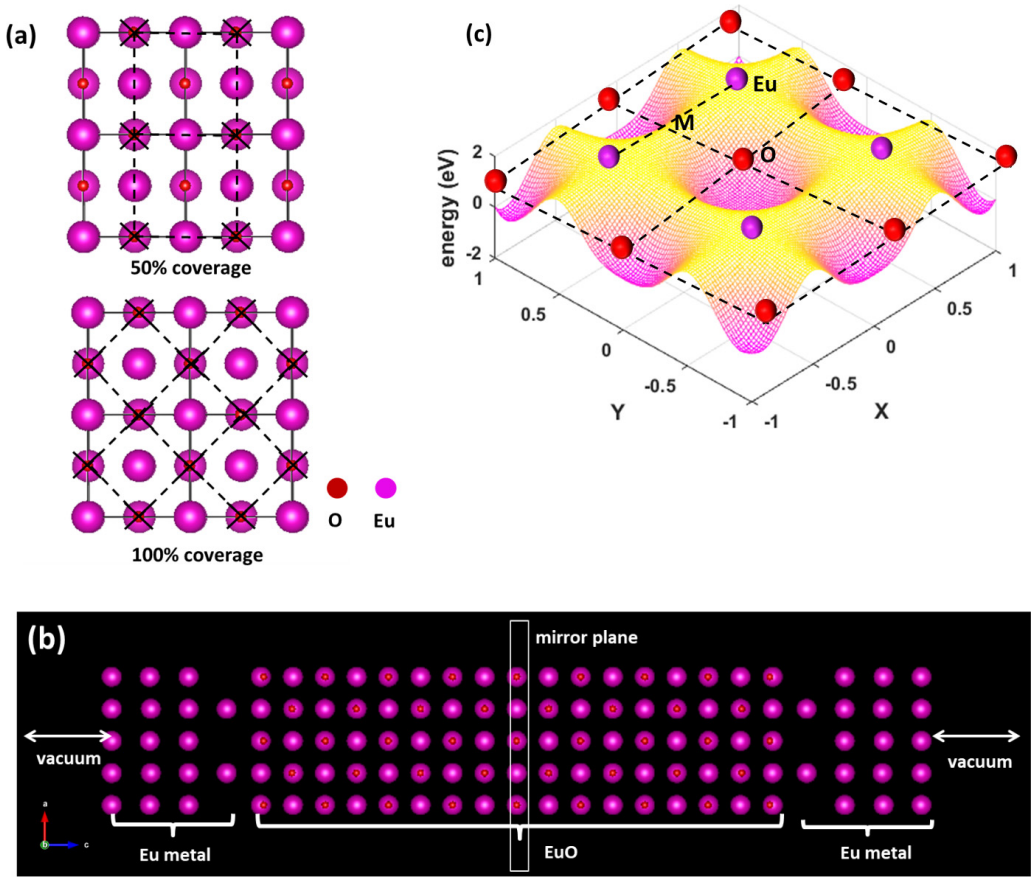

FIG. 1. (a) Top view of two possible Eu/EuO interfaces: (1) Eu layers experiencing 11.2% tensile strain on top of (001) EuO, with 50% coverage of surface O atoms; (2) Eu layers experiencing 18.9% compressive strain on top of 45°-rotated (001) EuO, with 100% coverage of surface O atoms. (b) The structural model of the type (3) hybrid heterostructure $(Eu)_2/(EuO)_{8.5.5}/(Eu)_2$ supercell. (c) Potential-energy surface of a Eu adatom on the $\sqrt{2} \times \sqrt{2}$ EuO surface. The middle point of the Eu-Eu distance is denoted with letter M.

approach and employ the GGA+U scheme for Eu in the metallic phase as well as in EuO. The $5s^2\,5p^6\,4f^7\,6s^2$ electrons (17 total electrons) are treated explicitly in the Eu pseudopotential and, as several authors have done before, we use an empirical value $U_f = 8.0\,\text{eV}$, which results in a band-gap value of 1.2 eV, close to what is measured [28–30], and a lattice constant of 5.18 Å for EuO [31]. Europium metal crystallizes in a bcc structure. It is antiferromagnetic at low temperature (Néel temperature of 91 K), with the magnetic ground state being a spin spiral [32,33]. For Eu metal, a different U value, $U_f = 5.0\,\text{eV}$, is used. As discussed below, this U value results in a position of the $4f$ peak for Eu metal that is in good agreement with spectroscopic measurements. Also, the calculated lattice constant for Eu metal of 4.59 Å agrees well with the measured value of 4.58 Å at room temperature and 4.56 Å below 100 K. For oxygen, $2s^2\,2p^4$ electrons are treated explicitly in the pseudopotential. We model the Eu/EuO system by designing a symmetric $(Eu)_2/(EuO)_{8.5}/(Eu)_2$ supercell (the subscript refers to the unit-cell number). Since experimentally Eu metal is deposited on top of EuO, we take EuO as the substrate and fix the lateral dimensions of the supercell to the lattice constant of EuO. However, there is a large lattice mismatch, and the actual positions at the interface of the metal ions relative to the oxide are not fully known. To find the most stable geometry of the Eu/EuO interface, we first model the early stages of Eu deposition on (001) EuO by placing one Eu adatom on top of the (001)-oriented EuO surface modeled with a $\sqrt{2} \times \sqrt{2} \times 5$ slab. A large vacuum region is inserted between the EuO slabs. As shown below, the lowest energy is obtained when Eu is placed directly above an O atom. Based on this result, we build two possible types of interfaces as shown in Fig. 1(a): (1) Eu layers experiencing 11.2% tensile strain on top of (001) EuO, with half of the oxygen atoms on the surface covered; (2) Eu layers experiencing 18.9% compressive strain on top of 45°-rotated (001) EuO, with all the oxygen atoms covered. For the first configuration, half of the surface O atoms have dangling bonds. For the second configuration, all O atoms on the EuO surface have full coordination, but Eu layers experience a higher strain [34]. The electronic structure of the second configuration appears to match experiment better (see Supplemental Material [35]), but the large strain may lead to unphysical results. Considering this, we chose to use a third interface configuration: a hybrid configuration where the interfacial Eu layer is under tensile strain and three Eu layers above are under compressive strain. After we set up the Eu metal configuration, we add eight EuO layers below the interface and then double the cell in the z direction to create a mirror symmetric slab. The lateral dimension of the supercell is 5.18 Å. The final structure is shown in Fig. 1(b).

Because the three Eu layers experience a highly compressive strain laterally, the distance between neighboring Eu layers in the z direction increases from 2.3 to 3.2 Å. In bulk, this causes the f and d bands to shift upwards in energy by 0.1 and 0.2 eV, respectively, with respect to the Fermi level. In a pure slab calculation for Eu metal (with the vacuum region), the work function increases from 2.51 to 2.56 eV as a result of strain. Thus, we believe, despite this limitation, the electronic structure effects of strain are minimal. The band alignment of a strain-free system is similar to that of a strained system (see Supplemental Material [35]). Therefore, the structure we adopt and the phenomena described here are reasonable. For the slab calculation, the vacuum thickness is 15 Å. Both slab and heterostructure structures are relaxed until the interatomic forces become smaller than 0.05 eV/Å. We use a plane-wave cutoff energy of 500 eV throughout this work. For the adatom slab calculations, we sample the Brillouin zone with a $4 \times 4 \times 1$ Monkhorst-Pack k-point grid [36]. For the heterostructure calculations, a $17 \times 17 \times 1k$-point grid is used.

In order to compare theory and experiment, we deposit Eu metal on EuO formed using oxygen scavenging of STO [13]. The oxygen scavenging method allows for crystalline EuO to be deposited on STO layers without the risk of overoxidizing the EuO film to form Eu_2O_3. The deposition is performed in a customized DCA 600 molecular beam epitaxy (MBE) system with a base pressure of 6×10^{-10} Torr. We prepare STO/Si pseudosubstrates using a modification of the Motorola process [37–39]. Eu metal is evaporated from an effusion cell with the cell temperature fixed at 530 °C, which has been determined to yield a Eu metal evaporation rate of ∼2.5 Å/min. The Eu evaporation rate is determined by measuring the thickness of epitaxial Eu_2O_3 films grown at the same effusion cell temperature using x-ray reflectometry, where we assume that the sticking coefficient of Eu is unity in excess oxygen environment. For this work, Eu metal is deposited on the STO surface at 20 °C. Due to oxygen scavenging of the STO layer, a self-limited epitaxial EuO layer of ∼3 nm is formed. Reflection high-energy electron diffraction (RHEED) is used to monitor the surface crystallinity changes as we go from the bare STO surface to crystalline rocksalt EuO and eventually to amorphous Eu metal. The Eu deposition is divided into multiple steps, each lasting 10 min. The deposition is paused at the end of each step in order to transfer the sample into an *in situ* XPS analysis chamber. The sample is then quickly moved back to the MBE growth chamber for the next deposition step. *In situ* XPS, with monochromated Al $K\alpha$ radiation and a VG Scienta R3000 hemispherical electron energy analyzer, is used to monitor the core levels of relevant elements as well as the valence-band spectrum after each deposition step. Eu metal starts to accumulate between 20 and 30 min deposition time, as indicated by the emergence of intensity at the Fermi level. This procedure allows us to see the evolution of the chemical and electronic structure of the sample as Eu is deposited. The layer compositions and thicknesses are inferred from a combination of the onset time of RHEED pattern changes, the deposition time dependence of the valence-band spectrum, and the attenuation of the substrate Ti $2p$ core-level spectrum. A summary of these measurements is shown in Figs. S4–S6 of the Supplemental Material [35]. From these data, we infer that at 20 °C substrate temperature our heterostructure consists of 3 nm of crystalline EuO and 6 nm of amorphous Eu metal after 60 min of Eu metal exposure. This also shows that the Eu metal sticking coefficient is about 0.6 in the absence of any surface reaction.

III. POTENTIAL-ENERGY SURFACE

In the bulk Eu bcc crystal structure, the shortest Eu-Eu bond length is 3.98 Å. Therefore, we consider a $\sqrt{2} \times \sqrt{2}$ (001) EuO slab to be large enough to model the Eu adatom (the periodic replicas are separated by 7.32 Å). To calculate the PES, we divide the surface simulation cell using an 8×8 grid and calculate total energy after the adatom is introduced at each grid point. In-plane motion of the adatom is forbidden while motion along the z direction is allowed, and the energy of the entire system is optimized. For the remaining points on the surface, the energy is interpolated using these 64 calculated values.

The PES is shown in Fig. 1(c). The potential-energy minimum is found to be above the O site and is 1.8 eV lower in energy than the maximum located on top of the Eu site. At the midpoint M along the Eu-Eu line, which is also the midpoint between two oxygen atoms, the potential energy is 0.1 eV lower than at the Eu site (maximum) but 1.7 eV higher than that at the O site. This suggests an energy barrier of 1.7 eV needs to be overcome in order to move between neighboring O sites. To estimate the time scale for Eu diffusion, we use the Arrhenius formula for kinetics $\frac{1}{\tau} = \nu e^{-E/kT}$, where τ is a time interval for Eu hopping, E is the energy barrier, and ν is an attempt frequency for the surface diffusion with the vibrational frequency of the adatom, usually on the order of $10^{12}\,s^{-1}$ [40]. As discussed below, Eu metal deposition is performed at room temperature (20 °C). With this formula, the time scale for hopping at room temperature between neighboring O sites is on the order of 10^{16} s. As for the interaction between the adatom and the surface, Eu would be strongly bound to oxygen on the (001) EuO surface. The adatom Eu-O bond length is 2.3 Å, 10% shorter than that in bulk EuO (2.6 Å). These results suggest that to model a stable interface, it may be sufficient to consider the Eu/EuO interface structures with Eu placed directly above the O atom, as shown in Fig. 1(b).

IV. ELECTRONIC STRUCTURE OF THE INTERFACE

First we consider the electronic structure of pure Eu metal theoretically, as the topic has not received much attention in the literature. Though the magnetic ground state is spiral, here we consider only the collinear and ferromagnetic state as we have only a few Eu layers. Wang *et al.* have recently studied the valence band of Eu metal using synchrotron photoemission [41]. The states at the Fermi level (E_F) are composed of Eu $5d$ states, and the $4f$ state is 2.1 eV below E_F in energy. Also, a broad feature around 5.2 eV below E_F is observed and labeled as having $6s$ character. We set the calculation parameters to closely match the experiment. Within the DFT+U formalism, the orbital energy ε_i' could be written as $\varepsilon_i' = \varepsilon_i + U(\frac{1}{2} - n_i)$, where ε_i is the orbital energy of the regular LDA/GGA functional, U is the Coulomb repulsion, and n_i is the orbital occupation [42]. With an

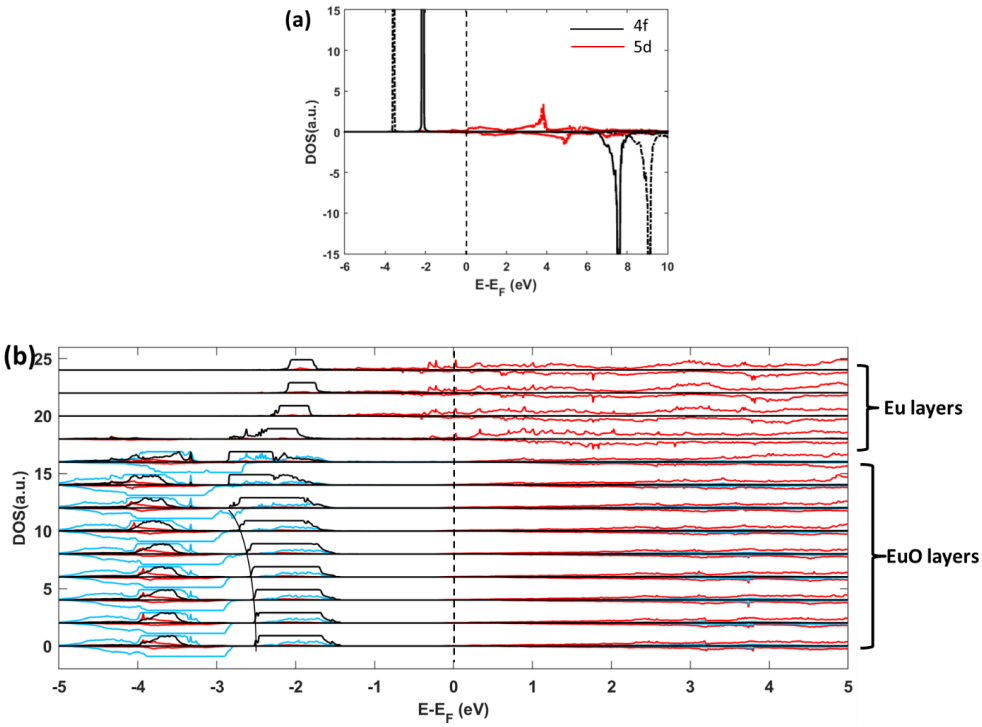

FIG. 2. (a) The orbital-projected density of states (DOS) of bulk Eu metal with different Hubbard-type U values. Solid and dashed lines represent results for $U = 5.0$ and 8.0 eV, respectively. (b) The orbital-projected DOS on specific atoms for each layer in the $(Eu)_2/(EuO)_{8.5}/(Eu)_2$ heterostructure. Only results of the upper half-cell are shown due to symmetry. Eu-f, Eu-d, O-p states are marked by black, red, and light blue, respectively.

increasing U value applied to the Eu $4f$ orbital, the occupied, spin-up $4f$ states shift down in energy, away from E_F, while the unoccupied, spin-down $4f$ states shift up in energy. Figure 2(a) shows the electronic structure of Eu metal computed using two values of U : $U_f = 5.0$ eV and $U_f = 8.0$ eV. The smaller U value indeed predicts a $4f$ spin-up peak at the higher energy. With $U_f = 8.0$ eV, the peak is 3.6 eV below E_F, while with $U_f = 5.0$ eV, the peak is about 2.1 eV below E_F, which agrees with the synchrotron photoemission results better. For metallic $5d$ states, only a slight difference is found between the results obtained with these two U values. This is because the hybridization between the $5d$ orbitals and the localized $4f$ orbitals is weak. For both U_f values, the magnetic moment of Eu is calculated to be 7.0 μ_B. Therefore, we adopt $U_f = 5.0$ eV for the Eu metal.

Let us now consider the band alignment at the Eu/EuO interface. In Fig. 2(b) we show the orbital-projected density of states (DOS) on specific atoms for each layer of the hybrid $(Eu)_2/(EuO)_{8.5}/(Eu)_2$ heterostructure. Owing to the mirror symmetry of the cell, only half of the simulation cell is shown. In the valence-band region, the localized spin-up $4f$ peak has a bandwidth of approximately 0.3 eV. At the interface, the Eu $4f$ peak is 2.2 eV below the Fermi energy, while for the other three Eu layers, the $4f$ peak is located at about 2 eV below the Fermi energy. This comes from the different Eu layers having different strain (see Supplemental Material [35]). The $4f$ peaks of EuO have a larger bandwidth of approximately 1 eV due to hybridization with the oxygen p states. By connecting the "front edge" of the spin-up $4f$ peak of each layer in Fig. 2(b) to guide the eye, we can see that the peak position continuously shifts up throughout the whole EuO region. Following this guiding line, we can see that at the interface, the $4f$ peak is 0.3 eV lower in energy compared with the $4f$ peak coming from deep in the bulk of EuO. This is a sign of a downward band bending, as the potential is low at the interface, increases gradually, and eventually reaches a plateau in the bulk of EuO. This causes the $4f$ peak from each layer to be distributed over a wider energy range, which should result in a significant asymmetric broadening that should be detectable in a photoemission experiment.

Figures 3(a) and 3(b) show the experimental XPS data for Eu step-by-step deposition on STO/Si pseudosubstrate at 20 °C. In Fig. 3(a) we show the valence-band (VB) XPS spectrum for a sample after 10 min of Eu deposition on the (001) STO surface. Only rocksalt EuO forms at this time as a result of oxygen scavenged from STO by Eu atoms. The EuO is crystalline as indicated by RHEED [43]. The Eu^{2+} $4f$ peak is observed at a binding energy of 2.2 eV, and the smaller and broader peak centered at 5 eV is from the oxygen $2p$ band. From 6 to 15 eV the spectrum is flat without any peaks, indicating that there is no Eu^{3+} present. This is important, as the formation of the sesquioxide Eu_2O_3, which is not ferromagnetic, could reduce the spin-filtering efficiency of a EuO barrier [37]. In Fig. 3(b), the VB spectrum of a sample after 60 min of Eu deposition is shown. We can see the presence of the metallic Eu spectrum. Due to the low deposition temperature resulting in low oxygen mobility through EuO, Eu is unable to continuously scavenge oxygen from STO. This limits the thickness of EuO to about 2 nm with Eu metal accumulating on top of the EuO. Compared with Fig. 3(a),

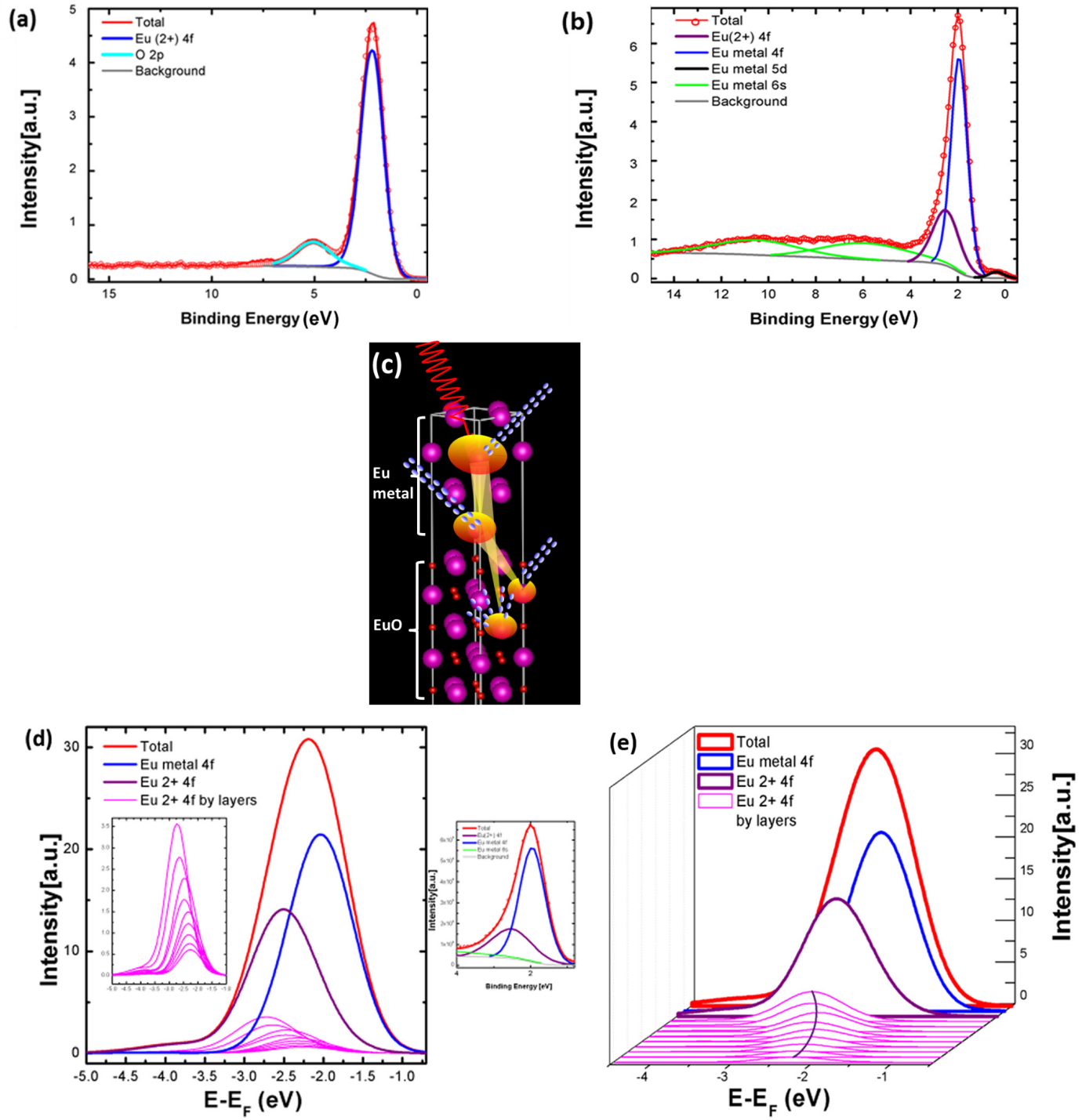

FIG. 3. (a) Valence-band XPS spectrum of 10 min Eu deposition on 2-nm STO/Si pseudosubstrate at 20 °C. This is consistent with the spectrum from bulk EuO. (b) Valence-band XPS spectrum of 60 min Eu deposition at 20 °C. A Eu/ EuO/STO/Si structure is formed. (c) A schematic diagram of XPS applied to our simulation cell. (d) The attenuated and broadened $4f$ DOS of the whole heterostructure ("calculated pseudo-XPS spectrum"). The Eu metal $4f$ DOS is marked as dark blue, the $4f$ DOS of each EuO layer is marked as magenta, the total EuO $4f$ DOS is marked as violet, and the total $4f$ DOS is marked as red. The inset gives the $4f$ DOS of each EuO layer on a larger scale. (e) A three-dimensional representation of the "calculated-pseudo-XPS spectrum." Here the spectrum of each layer is shown separately along the y direction. The peak position of $4f$ EuO DOS of each layer is connected with a violet line.

which shows the spectrum of pure EuO, several other features can be seen due to the presence of Eu metal. There is a clear, nonzero intensity at the Fermi energy appearing as a small step, corresponding to the partially occupied Eu $5d$ band, which is a clear signature of the metal. This feature emerges at 30 min deposition time and increases in relative intensity as more Eu is deposited. The Eu $4f$ feature becomes asymmetric and now is required to fit with two components instead of

one, as shown in more detail in Fig. 3(b). The $4f$ component at 2.2 eV is the Eu^{2+} signal from EuO, while the other $4f$ component at 1.9 eV is interpreted as a Eu metal $4f$ signal. As more Eu metal is deposited, the $4f$ peak clearly shifts toward lower binding energy, because the Eu component at 1.9 eV is increasing in intensity while the EuO component at 2.2 eV is getting progressively buried. This is a clear indication that at some point oxygen is no longer able to diffuse through existing EuO at this temperature and Eu metal begins to accumulate atop the EuO layer. There are also additional broad and weak features in the 4–14 eV binding energy range that appear in the metallic phase that quickly bury the EuO oxygen $2p$ peak. These are likely related to Eu $6s$ electrons in Eu metal as seen in synchrotron measurements [41]. It should be noted that because oxygen is supplied via diffusion from STO, there is likely a slight reduction in oxygen content in the film as the EuO grows thicker. It is therefore likely that a slightly oxygen-deficient EuO layer is present right at the interface up to the composition range of the EuO phase, which is reported to be not more than 1 mol% [44,45]. However, since oxygen solubility in Eu is extremely small [46], any oxygen not reacting to form EuO is likely to segregate to the (oxygen-deficient) EuO side of the interface, resulting in Eu metal starting to accumulate once the scavenging depth is reached. This self-limiting behavior of EuO thickness is also observed in the recent detailed study of the EuO oxygen scavenging process by Lomker and Muller [47].

To facilitate the comparison with the experiment, we broaden the calculated $4f$ DOS of each layer using Gaussian convolution. A schematic of the XPS experiment modeled in our simulation cell is shown in Fig. 3(c). Based on the width of experimental XPS spectra, we choose a FWHM parameter $\sigma = 0.90$ eV. Considering the inelastic scattering in an XPS measurement, we attenuate the $4f$ DOS for each layer by a factor of $e^{-(d/L)}$, where d is the depth of the layer and L is the inelastic mean free path. The inelastic mean free path of a $4f$ electron (kinetic energy of ~1480 keV) is 23 and 31 Å for EuO and Eu, respectively, as calculated using the TPP-2M formula [48]. We then add up the attenuated and broadened DOS of each layer as the "calculated pseudo-XPS spectrum" and show it in Fig. 3(d). The $4f$ DOS of each EuO layer (magenta lines) clearly shows the band bending. The peak position of the interfacial EuO $4f$ DOS is 2.7 eV and that of the bulklike EuO $4f$ DOS is at 2.3 eV. This leads to the overall broadening of the EuO $4f$ spectra. For the Eu metal $4f$ state, the peak position is 2.1 or 0.4 eV higher compared to that of the total EuO $4f$ DOS. This is close to the experimental measurement (0.3 eV), and the 0.1-eV discrepancy can be ascribed to the EuO band-gap difference between the calculation and experiment. As can be seen from the experimental XPS spectrum, the Eu metal component is much more dominant, as EuO is buried and the corresponding signal has been largely attenuated due to the longer travel distance of the photoelectrons. We observe that for the structure of two Eu metal layers over 8.5 layers of EuO, the EuO-to-Eu signal intensity ratio from the pseudo-XPS spectrum is ~0.7. We also observe that for another structure of two Eu metal layers over 12.5 EuO layers, the EuO/Eu ratio is ~1.1 (see Supplemental Material, Fig. S3(b) [35]). On the other hand, it also influences the spacing between the total $4f$ peak and Eu metal $4f$ peak. In experiment, the peak position of the total $4f$ spectrum is very close to that of the Eu metal $4f$ spectrum, while in the calculation, the former is separated by 0.2 eV from the latter. We show the spectrum of each EuO layer separately in Fig. 3(e). Following the violet line indicating the peak position of the EuO $4f$ contribution, the band bending across the EuO layers can be clearly seen. Overall, accounting for the contributions by both Eu metal and EuO, the total $4f$ peak spectral width increases to 1.1 eV. This is comparable to the 0.8 eV width observed in experiment.

V. CHARGE TRANSFER AT THE Eu/EuO INTERFACE

With a $(Eu)_2/(EuO)_{12.5}/(Eu)_2$ supercell (see Supplemental Material [35]), one can gain additional insight into the band alignment from the spin-up $5d$ and $4f$ DOS contour plot in the energy vs EuO layer coordinate plane shown in Fig. 4(a). We note that due to a large spin-splitting of the EuO $5d$ band, the spin-down $5d$ band bottom stays well above the Fermi level in all EuO layers. Also, since the spin-down $4f$ band lies far above the Fermi level, we show only the contour plot for the spin-up component. At the interfacial EuO layer, the conduction-band bottom is 0.4 eV below E_F. Charge transfer from the Eu metal leads to degeneracy of these EuO layers. Deeper in the oxide, however, the $5d$ band bottom gradually approaches E_F, and in the bulklike region EuO recovers its insulating character. As Fig. 4(a) shows, the spin-polarized conductive region spreads over a length of about five to six atomic layers of EuO, corresponding to a distance of 15 Å. This can also be seen if we plot the charge distribution in the energy window from E_F to 0.4 eV below E_F shown in Fig. 4(b). A large amount of charge is seen in the first two EuO layers near the interface, which then decays and completely disappears by the seventh EuO layer.

To explore the charge transfer from Eu metal to EuO, we calculate the work function (WF) of Eu (Φ_M), and the electron affinity (χ_S) and ionization potential (IP) of EuO. These values are evaluated using the isolated slab calculations for each material. Φ_M is determined as the difference between the electrostatic potential in the vacuum region (V_{vac}) and E_F of the Eu slab, while χ_S and IP are determined as the difference between V_{vac} and the conduction-band bottom and valence-band top of the EuO slabs, respectively. Previous work has shown that to obtain a converged value of the work function, a thick metal slab needs to be considered [49,50]. Thus, in the calculation, we use 13 atomic layers for both the Eu and EuO slabs. The calculated Φ_M of 2.56 eV is in good agreement with the photoemission measurement of 2.5 eV [51]. For EuO, χ_S is calculated to be 1.42 eV, comparable with the experimentally measured value of 1.7 eV [52]. The energy gap between the conduction-band bottom and the valence Eu $4f$ band top is measured to be 1.1 eV [52], while in the calculation, the band gap is 1.27 eV. This gives a calculated IP value of 2.7 eV, which is close to the experimental value of 2.8 eV [52]. As shown in Fig. 5(a), before contact, E_F of Eu is in the gap of EuO, 0.14 eV higher than the valence-band top. This is quite different from what has been shown previously for the interface of Pt and EuO [18]. There, the valence-band top of EuO was 2.59 eV higher than E_F of Pt, which resulted in charge flow from EuO to Pt, inducing a spin-polarized

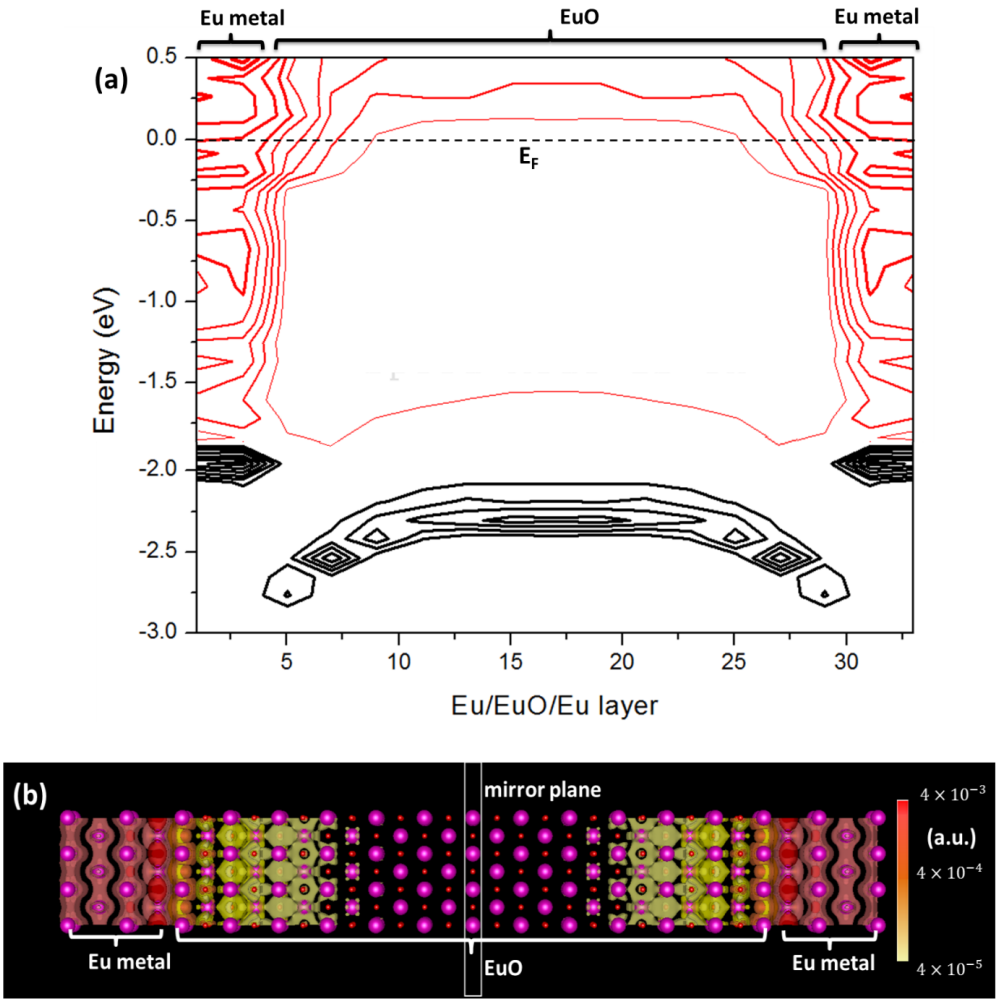

FIG. 4. (a) Spin-up $5d$ (red) and $4f$ (black) DOS contour plot as a function of energy and $(Eu)_2/(EuO)_{12.5}/(Eu)_2$ heterostructure layer. (b) Charge isosurface of the heterostructure in the energy range $(-0.4\ \text{eV}, 0)$ relative to E_F.

two-dimensional hole gas (2DHG) in EuO near the interface [18].

As shown in Fig. 5(b), after Eu and EuO are brought into contact, electrons flow from Eu to EuO and the band bending is similar to what happens at the interface of a low-work-function metal and an n-type semiconductor. In the bulklike region of EuO, E_F is close to but below the conduction-band bottom of EuO. This charge transfer does not obey the Schottky-Mott rule, since E_F is initially 1.13 eV below the conduction band of EuO. However, at the metal-

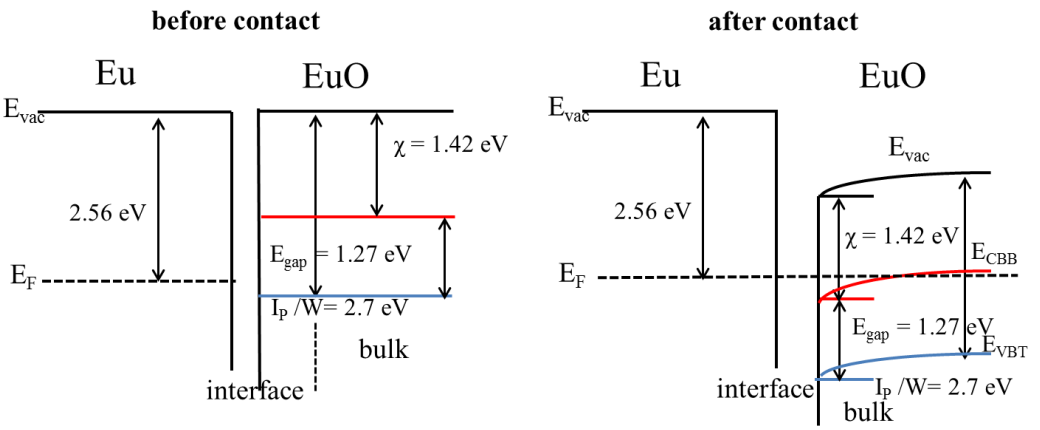

FIG. 5. Energy-band diagram of Eu and EuO (a) before contact and (b) after contact.

semiconductor interface, the band alignment often follows the metal-induced gap states (MIGS) model [53]. The model suggests that the metal E_F is pinned at the charge neutrality level (CNL) of the semiconductor [54–58]. One then expects charge transfer to occur via filling the evanescent states in the EuO band gap. However, as shown in Fig. 2(b), the electronic structure does not show any in-gap states at the interfacial EuO layer. Recently, Jutong *et al.* reported the complex band structure for EuO and found that for the spin-up channel, the evanescent state with Δ_1 symmetry has a short imaginary vector of $0.21\,\text{Å}^{-1}$ at the branch point [1]. This corresponds to a long decay length of 4.8 Å for the evanescent state [59]. We can use the density of Eu $4d$ states in each layer to estimate an exponential decay length of 5.8 Å, which is close to the 4.8 Å value calculated from the imaginary wave vector [1]. Importantly, the CNL corresponding to this evanescent state is 0.2 eV higher (!) in energy than the conduction-band bottom. Note that this is rather unusual, since in the typical case the CNL lies within the insulator band gap. Reviewing our situation, the Fermi level is 0.4 eV higher than the bottom of the oxide spin-up $5d$ band at the interface, roughly at the same level as the CNL predicted by Jutong *et al.* [14]. The numerical discrepancy likely stems from the difference in the theoretical electronic structure. We conclude that the charge transfer from Eu to EuO found in our DFT calculation agrees with the MIGS model, assuming the CNL of EuO is associated with the spin-up evanescent state as reported in Ref. [14]. On the other hand, Lukashev *et al.* also investigated the complex band structure of EuO [60], and they reported a different CNL that is 0.4 eV below the conduction-band bottom for a 0.9-eV band gap. The Δ_1 evanescent state also has a shorter imaginary vector of $0.12\,\text{Å}^{-1}$. Our results appear to be in better agreement with the model of Jutong *et al.* [14].

VI. WETTING CONDITIONS

From the deposition point of view, it is important to know whether Eu is able to wet EuO. Thermodynamically, the wetting condition is $\gamma_{\text{substrate}} > \gamma_{\text{interface}} + \gamma_{\text{film}}$, where γ is the surface or interfacial energy. In our calculation, EuO is the substrate and Eu is the film. For the surface energy calculation, we take the (001)-oriented EuO and (001)-oriented Eu slabs and estimate the surface energy as $\gamma_{\text{surface}} = \frac{1}{2A}(E_{\text{slab}} - NE_{\text{bulk}})$, where N is the number of unit cells in the slab and E is the total energy of the slab or bulk, respectively. The interfacial energy can be calculated as $\gamma_{\text{interface}} = \frac{1}{2A}(E_{\text{Eu/EuO}} - N_{\text{Eu}}E_{\text{Eu-bulk}} - N_{\text{EuO}}E_{\text{EuO-bulk}})$, where N is the number of corresponding unit cells in the Eu/EuO heterostructure and $E_{\text{Eu/EuO}}$ is the total energy of the heterostructure. With this approach, Eu and EuO surface energies are calculated to be 0.51 and $0.48\,\text{J/m}^2$, respectively, and the interfacial energy is calculated to be $0.37\,\text{J/m}^2$. This obviously doesn't meet the wetting condition. The reason is that the surface energy of EuO is surprisingly low compared with other metal oxides used as substrates. For example, the surface energy of MgO is $1.15\,\text{J/m}^2$ [61]. This suggests that Eu on EuO grows as three-dimensional islands following the Volmer-Weber growth mode. This is in agreement with our RHEED experiments, which show three-dimensional diffraction spots. As we discuss in the Supplemental Material [35], strain does not affect the band alignment significantly, so the results are applicable to the discussion of a metal film obtained through the merging of islands. Also, to model the interface using first-principles methods, one has to make a periodic arrangement to model the interface. As a side comment, the results suggest that high-quality films of EuO can be grown epitaxially on many oxide substrates, as it is favored by its very low surface energy. The formation of a suboxide is a well-known problem for Schottky barriers with large work-function metals [62–64], and it is likely an oxygen-deficient EuO transition layer can be formed as oxygen diffuses from the substrate. The theoretical analysis is complicated and would be a topic of future investigation for this material.

VII. CONCLUSIONS

In summary, by combining theoretical calculations with *in situ* XPS measurements, we studied the atomic and electronic structure of the Eu/EuO interface. The atomic configuration with Eu directly above the O atom with 45°-rotated (001) EuO is the most favorable. Once the metal and oxide are brought into contact, the Fermi level of Eu lines up with the charge neutrality level of EuO arising from the spin-up evanescent state. Interestingly, this level appears to be above the conduction-band bottom of EuO, in agreement with recent calculations [1]. Consequently, charge transfer of the $5d$ electrons from the Eu metal ∼15 Å inside EuO induces a downward band bending near the interface. This downward band bending is confirmed experimentally by analyzing the XPS spectra of the Eu $4f$ peaks and their broadening at the Eu/EuO interface.

ACKNOWLEDGMENTS

This research was partially supported by the National Science Foundation through the Center for Dynamics and Control of Materials: an NSF MRSEC under Cooperative Agreement No. DMR-1720595 and by the Air Force Office of Scientific Research under Grant No. FA9550-18-1-0053.

[1] P. Wachter, CRC Crit. Rev. Solid State Sci. **3**, 189 (1972).
[2] J. C. Suits, B. E. Argyle, and M. J. Freiser, J. Appl. Phys. **37**, 1391 (1966).
[3] J. H. Greiner and G. J. Fan, Appl. Phys. Lett. **9**, 27 (1966).
[4] N. M. Souza-Neto, D. Haskel, Y.-C. Tseng, and G. Lapertot, Phys. Rev. Lett. **102**, 057206 (2009).
[5] A. Melville, T. Mairoser, A. Schmehl, T. Birol, T. Heeg, B. Holländer, J. Schubert, C. J. Fennie, and D. G. Schlom, Appl. Phys. Lett. **102**, 062404 (2013).
[6] M. W. Shafer and T. R. McGuire, J. Appl. Phys. **39**, 588 (1968).
[7] Y. Shapira, S. Foner, and T. B. Reed, Phys. Rev. B **8**, 2299 (1973).

[8] T. Penney, M. W. Shafer, and J. B. Torrance, Phys. Rev. B **5**, 3669 (1972).

[9] G. Petrich, S. Von Molnár, and T. Penney, Phys. Rev. Lett. **26**, 885 (1971).

[10] A. Schmehl, V. Vaithyanathan, A. Herrnberger, S. Thiel, C. Richter, M. Liberati, T. Heeg, M. Röckerath, L. F. Kourkoutis, S. Mühlbauer, P. Böni, D. A. Muller, Y. Barash, J. Schubert, Y. Idzerda, J. Mannhart, and D. G. Schlom, Nat. Mater. **6**, 882 (2007).

[11] D. V. Averyanov, Y. G. Sadofyev, A. M. Tokmachev, A. E. Primenko, I. A. Likhachev, and V. G. Storchak, ACS Appl. Mater. Interfaces **7**, 6146 (2015).

[12] D. V. Averyanov, C. G. Karateeva, I. A. Karateev, A. M. Tokmachev, A. L. Vasiliev, S. I. Zolotarev, I. A. Likhachev, and V. G. Storchak, Sci. Rep. **6**, 22841 (2016).

[13] A. B. Posadas, K. J. Kormondy, W. Guo, P. Ponath, J. Geler-Kremer, T. Hadamek, and A. A. Demkov, J. Appl. Phys. **121**, 105302 (2017).

[14] N. Jutong, I. Rungger, C. Schuster, U. Eckern, S. Sanvito, and U. Schwingenschlögl, Phys. Rev. B **86**, 205310 (2012).

[15] T. S. Santos, J. S. Moodera, K. V. Raman, E. Negusse, J. Holroyd, J. Dvorak, M. Liberati, Y. U. Idzerda, and E. Arenholz, Phys. Rev. Lett. **101**, 147201 (2008).

[16] E. Negusse, J. Holroyd, M. Liberati, J. Dvorak, Y. U. Idzerda, T. S. Santos, J. S. Moodera, and E. Arenholz, J. Appl. Phys. **99**, 08E507 (2006).

[17] T. S. Santos and J. S. Moodera, Phys. Rev. B **69**, 241203(R) (2004).

[18] K. D. Fredrickson and A. A. Demkov, J. Appl. Phys. **119**, 095309 (2016).

[19] D. F. Förster, J. Klinkhammer, C. Busse, S. G. Altendorf, T. Michely, Z. Hu, Y.-Y. Chin, L. H. Tjeng, J. Coraux, and D. Bourgault, Phys. Rev. B **83**, 045424 (2011).

[20] S. Schumacher, D. F. Förster, F. Hu, T. Frauenheim, T. O. Wehling, and T. Michely, Phys. Rev. B **89**, 115410 (2014).

[21] G. Kresse and J. Furthmüller, Comput. Mater. Sci. **6**, 15 (1996).

[22] G. Kresse and J. Furthmüller, Phys. Rev. B **54**, 11169 (1996).

[23] J. P. Perdew and A. Zunger, Phys. Rev. B **23**, 5048 (1981).

[24] J. P. Perdew, K. Burke, and M. Ernzerhof, Phys. Rev. Lett. **77**, 3865 (1996).

[25] I. Turek, J. Kudrnovský, M. Diviš, P. Franek, G. Bihlmayer, and S. Blügel, Phys. Rev. B **68**, 224431 (2003).

[26] V. I. Anisimov, J. Zaanen, and O. K. Andersen, Phys. Rev. B **44**, 943 (1991).

[27] J. Kuneš and R. Laskowski, Phys. Rev. B **70**, 174415 (2004).

[28] P. Larson and W. R. L. Lambrecht, J. Phys.: Condens. Matter **18**, 11333 (2006).

[29] J. Kuneš, W. Ku, and W. E. Pickett, J. Phys. Soc. Japan **74**, 1408 (2005).

[30] J. Lee, N. Sai, and A. A. Demkov, Phys. Rev. B **82**, 235305 (2010).

[31] P. G. Steeneken, L. H. Tjeng, I. Elfimov, G. A. Sawatzky, G. Ghiringhelli, N. B. Brookes, and D.-J. Huang, Phys. Rev. Lett. **88**, 047201 (2002).

[32] N. G. Nereson, C. E. Olsen, and G. P. Arnold, Phys. Rev. **135**, A176 (1964).

[33] A. H. Millhouse and K. A. McEwen, Solid State Commun. **13**, 339 (1973).

[34] A. Posadas, J.-B. Yau, C. H. Ahn, J. Han, S. Gariglio, K. Johnston, K. M. Rabe, and J. B. Neaton, Appl. Phys. Lett. **87**, 171915 (2005).

[35] See Supplemental Material at http://link.aps.org/supplemental/10.1103/PhysRevMaterials.3.094403 for structural models, electronic structures, pseudo-XPS spectra for different Eu/EuO heterostructures, and evolution of RHEED and XPS spectra.

[36] J. D. Pack and H. J. Monkhorst, Phys. Rev. B **16**, 1748 (1977).

[37] R. A. McKee, F. J. Walker, and M. F. Chisholm, Phys. Rev. Lett. **81**, 3014 (1998).

[38] Y. Wei, X. Hu, Y. Liang, D. C. Jordan, B. Craigo, R. Droopad, Z. Yu, A. Demkov, J. L. Edwards, and W. J. Ooms, J. Vac. Sci. Technol., B **20**, 1402 (2002).

[39] H. Li, X. Hu, Y. Wei, Z. Yu, X. Zhang, R. Droopad, A. A. Demkov, J. Edwards, K. Moore, W. Ooms, J. Kulik, and P. Fejes, J. Appl. Phys. **93**, 4521 (2003).

[40] H. Brune, Surf. Sci. Rep. **31**, 125 (1998).

[41] X.-X. Wang, H.-N. Li, W.-H. Zhang, and F.-Q. Xu, J. Phys.: Condens. Matter **19**, 096001 (2007).

[42] V. I. Anisimov, F. Aryasetiawan, and A. I. Lichtenstein, J. Phys.: Condens. Matter **9**, 767 (1997).

[43] W. Guo, A. B. Posadas, S. Lu, D. J. Smith, and A. A. Demkov, J. Appl. Phys. **124**, 235301 (2018).

[44] M. W. Shafer, J. B. Torrance, and T. Penney, J. Phys. Chem. Solids **33**, 2251 (1972).

[45] A. Mauger and C. Godart, Phys. Rep. **141**, 51 (1986).

[46] P. R. Subramanian, Eu-O (europium-oxygen), in *Binary Alloy Phase Diagrams*, 2nd ed., edited by T. B. Massalski (ASM International, Materials Park, OH, 1990), Vol. 2, pp. 1665–1666.

[47] P. Lomker and M. Muller, Phys. Rev. Mater. **3**, 061401(R) (2019).

[48] S. Tanuma, C. J. Powell, and D. R. Penn, Surf. Interface Anal. **36**, 1 (2004).

[49] N. E. Singh-Miller and N. Marzari, Phys. Rev. B **80**, 235407 (2009).

[50] L. Gao, J. Souto-Casares, J. R. Chelikowsky, and A. A. Demkov, J. Chem. Phys. **147**, 214301 (2017).

[51] D. E. Eastman, Phys. Rev. B **2**, 1 (1970).

[52] D. E. Eastman, Phys. Rev. B **8**, 6027 (1973).

[53] V. Heine, Phys. Rev. **138**, A1689 (1965).

[54] S. G. Louie and M. L. Cohen, Phys. Rev. B **13**, 2461 (1976).

[55] C Tejedor, F. Flores, and E. Louies, J. Phys. C Solid State Phys. **10**, 2163 (1977).

[56] J. Tersoff, Phys. Rev. Lett. **52**, 465 (1984).

[57] J. Tersoff, Phys. Rev. B **30**, 4874 (1984).

[58] W. Mönch, Phys. Rev. Lett. **58**, 1260 (1987).

[59] A. A. Demkov, L. R. C. Fonseca, E. Verret, J. Tomfohr, and O. F. Sankey, Phys. Rev. B **71**, 195306 (2005).

[60] P. V. Lukashev, A. L. Wysocki, J. P. Velev, M. van Schilfgaarde, S. S. Jaswal, K. D. Belashchenko, and E. Y. Tsymbal, Phys. Rev. B **85**, 224414 (2012).

[61] A. R. C. Westwood and D. L. Goldheim, J. Appl. Phys. **34**, 3335 (1963).

[62] A. A. Demkov, Phys. Rev. B **74**, 085310 (2006).

[63] A. O'Hara, G. Bersuker, and A. A. Demkov, J. Appl. Phys. **115**, 183703 (2014).

[64] A. O'Hara and A. A. Demkov, Appl. Phys. Lett. **104**, 211909 (2014).